Tuning Deposition of Magnetic Metallic Nanoparticles from Periodic Pattern to Thin Film Entrainment by Dip Coating Method

Julien Dugay, Reasmey Phary Tan, Anais Loubat, Lise-Marie Lacroix, Julian Carrey, Pier-Francesco Fazzini, Bruno Chaudret, Marc Respaud

Tuning Deposition of Magnetic Metallic Nanoparticles from Periodic Pattern to Thin Film Entrainment by Dip Coating Method

J.Dugay,* R.P.Tan, A.Loubat, L.-M. Lacroix, J.Carrey,* Pier F. Fazzini, B.Chaudret, and M.Respaud

Laboratoire de Physique et Chimie des Nano-Objets, Université de Toulouse; INSA, UPS, 135, av. de Rangueil, F-31077 Toulouse, France CNRS; LPCNO, F-31077 Toulouse, France

E-mail: julien.dugay@gmail.com; julian.carrey@insa-toulouse.fr

Abstract

In this paper, we report the self-assembly of chemically synthesized metallic CoFe nanoparticles (NPs) from periodic pattern to thin film. NPs depositions were carried out inside a coupled glovebox-sputtering system to prevent NP oxidation and to tune the surface energy of the substrate through oxygen plasma treatment. A home-made dip coating setup allowing the vertical withdrawal of substrate from the colloidal suspension was used. We have systematically investigated the effects of NP concentration, withdrawal speed, nature (amino and acid groups) and amount of surfactants in suspension on the quality of the deposit on hydrophilic substrates (SiO_2 or Au). The stripe thickness, width and spacing, formed by the deposit, can be controlled by the NP concentration and the withdrawal speed. The surfactant concentration generally tends to decrease the NP coverage, except for amine which induced an improved coverage on silica substrate. We report here for the first time that dip coating is a suitable and reproducible technique to deposit magnetic metallic NPs over large areas from stripes pattern to thin films entrainment.

Introduction

Self-assembly is a physical concept present in Nature from atomic scale to large-scale structures of the universe. Such phenomenon can be defined as the self-assembly of similar entities in patterns or structures, without any human intervention, but in a controlled environment.[1] Nowadays, the recent developments in colloidal synthesis allows the growth and the self-assembly of artificial nanometer-scale metallic, semiconductor, and/or magnetic building blocks thanks to a fine tuning of NP morphological characteristic such as size, size-distribution and aspect ratio, and their physico-chemical properties governed by capping surfactants.[2]

Thanks to these unprecedented properties, magnetic NPs (MNPs) may be used for spintronics devices applications.[3,4] For instance a new type of magnetoresistance[5] and tunneling magnetoresistance (TMR) up to room temperature[6] have been recently observed in MNPs surrounded by organic ligands.

However, a crucial issue for such applications is the perfect control of MNPs deposit directly onto prefabricated electrodes in form of chains, arrays, and networks.[7] Such a control would allow on one hand, to tune the strength of the dipolar interactions between MNPs and thus increase the amplitude of the TMR.[8] We emphasize that to observe TMR in MNPs assemblies, drastic precautions against oxidation need to be taken.[6] On the other

hand, the control could also permits to study the influence of dimensionality and structural disorder on transport mechanism and therefore on the resulting magneto-transport properties.[9,10]

One way to integrate the NPs into patterned devices is based on physical and/or chemical templates, obtained by lithography,[11,12] microcontact printing,[13–16] micro-injection molding in capillaries,[17] dip pen lithography,[18,19] elimination lithography on self-assembled monolayers[20] or a combination of such approaches.[21,22]

Nevertheless, the one-step self-assembly of NPs on solid substrates directly from colloidal solution is highly desirable. To date, several strategies have been developed: drop-casting of NP suspension on solid substrates[23,24] or at the surface of an immiscible polar organic subphase,[25,26] langmuir-blodgett method,[27,28] convective-self assembly[29,30] or spin coating.[31]

In spite of extensive efforts, a direct deposition of NPs on solid surfaces with controlled arrangements - from stripes pattern to thin film entrainment - with tunable spacing, thickness and organization remains a challenge, especially when metallic magnetic nano-objects are involved. Indeed, to prevent NP from oxidation, the deposition based on polar organic subphase should be avoided while the atmosphere should be strictly controlled. Glovebox could enable such a control, however, space limitation and handling difficulty arisen. To our knowledge, no report on a controlled deposit method compatible with the metallic character of magnetic NPs assembly has been reported so far.

MNPs can be synthesized following various method,[32] one of which being the organometallic approach, which consists in the decomposition of a metal complex thanks to a reducing agent under mild conditions in presence of organic surfactants.[33] The final MNP is surrounded by surfactants which prevent their aggregation and ensure their stabilization in organic solvents with fairly low polarity.[34] An excess amount of surfactants is usually needed to insure the stabilization of the colloidal solution, thus, the uncoordinated surfactants can interact with the substrate and modify the morphology of the deposits.[35]The surfactants also affect the suspension properties such as evaporation rate, surface tension and colloidal/self-assembly behavior. The exact composition of the solution (amount and nature of surfactants) varying slightly with the synthesis, the detailed study of the influence of deposit parameter must be performed on the very same MNP batch.

Here we present the self-assembly of chemically synthesized metallic CoFe MNPs carried out with a home-made dip coating setup placed directly inside a coupled glovebox-sputtering system. Such a configuration preserves the good properties of the MNPs during the deposition while permitting the modulation of the interfacial energy of the substrates by oxygen plasma treatment. CoFe MNPs were synthesized by an organometallic approach in presence of amine and acid as surfactants. High yield and reproducibility were obtained. Such features permit to perform several experiments with the same batch in order to figure out the impact of the different key parameters. MNP concentration, withdrawal speed, nature and amount of surfactants in suspension and substrate surface state have a strong influence on the self-assembly process and allow controlling the nature of the deposit from stripes to thin film entrainment.

Experimental Section

Materials and Methods

Chemicals and materials. Chemicals and materials. All syntheses were prepared and purified under argon or dihydrogen using Fischer-Porter bottles techniques, a glove box and argon/vacuum lines. Mesithylene (99 %), tetrahydrofurane (THF, 99 %), were purchased from VWR Prolabo and distilled and degassed through three freeze-pump-thaw cycles. Hexadecylamine (HDA, 99 %), oleic acid (OA, 99 %) and stearic acid (SA, 99 %), were purchased from Sigma-Aldrich, iron(0)pentacarbonyl ($Fe(CO)_5$, 99,5%) from Acros organics and cyclooctadiene-cyclooctenyl ($Co(\eta^3 - C_8H_{13})(\eta^4 - C_8H_{12})$, 99 %) from Nanomeps and used as received.

Fabrication and preparation of the substrates. Standard photolithography was used to make gold electrodes (5 nm Ti/30 nm Au) on 0.25 cm^2 squares silicon wafers covered by a 300 nm layer

of thermally grown silica (SiO_2). Resina layer used to protect the substrates was removed with acetone, ethanol and deionized water and dried under nitrogen flow. UV ozone treatment of 15 min render them hydrophilic prior to their introduction in the glove box.
The surface wettability was characterized by contact angle measurements performed at room temperature with a GBX Digidrop. Each contact angle represents an average value of three measurements on different sample areas. Oxygen plasma could be used to modulate the surface energy of substrates stocked at least one day in advance in the glovebox, using a MP450s Plassys system coupled to the glove box. The working pressure was maintained at 8 mTorr, and a flow rate of 4 and 20 sccm respectively for argon and oxygen has been used with under 10W RF power.

Synthesis and characterization of CoFe MNPs. Core/shell carbide CoFe MNPs were prepared according to a modified published procedure.[36] In brief, $Co(\eta^3 - C_8H_{13})(\eta^4 - C_8H_{12})$ (1 mmole, 278 mg) was mixed with amine (HDA, 1 mmole, 242 mg) and acids (SA, 1 mmole, and OA, 1 mmole) in 10mL of Mesitylene. The reaction was stirred magnetically for 10 min. $Fe(CO)_5$ (2 mmole, 280μL) was then injected and 40 mL of Mesitylene added. The reaction is pressurized under 3 bars of dihydrogen and let to react at 150 °C for 48h. To remove excess surfactants, three washing process and magnetic separation using mesitylene were used, the NP solution was then evaporated under vacuum to get a dried powder.

A droplet of a colloidal suspension of CoFe MNPs was deposited inside a glovebox on covered holey copper grids. The latters were then characterized by TEM (transmission electron microscopy), HRTEM (high-resolution TEM), STEM-HAADF (scanning transmission electron microscopy using a high angle annular dark field detector) and EELS (electron energy loss spectroscopy). XRD (X-ray diffraction) and Mössbauer spectroscopy were carried out on a powder of CoFe MNPs that were prepared and sealed under an argon atmosphere.
TEM image (see Figure S1) of the MNPs was recorded with a JEOL-JEM 1011F, operating at 100 kV. The polydispersity in size was calculated from the size measurements of more than 2000 NPs using ImageJ software.[37]
STEM-HAADF observations (see Figure S2 (**a-b**) and EELS analysis (**c**)) were carried out at the LMA laboratory in Zaragoza, using a Cs corrected Titan Microscope equipped with an XFEG source.
XRD measurements (see Figure S2 (**d**)) were performed on a PANalytical Empyrean diffractometer using Co-Kα radiation at 45 KV and 40 mA.
The iron state and its environment (see Figure S3) were analyzed by Mössbauer spectroscopy (WISSEL, 57Co source).

Deposit of CoFe MNPs. Every steps were performed in the coupled glovebox-sputtering system under inert gas (Ar) to prevent NPs from oxidation. The MNPs were redispersed in Tetrahydrofurane (THF), solvent suitable for dip-coating deposit thanks to its low boiling point (66° C[38])[39] and surface tension (28.10^{-3} N.m[38]).[40]Colloidal solution with desired concentration were obtained from MNP powder diluted in the appropriate volume of solvent under ultrasonic bath (15 min, 40° C).

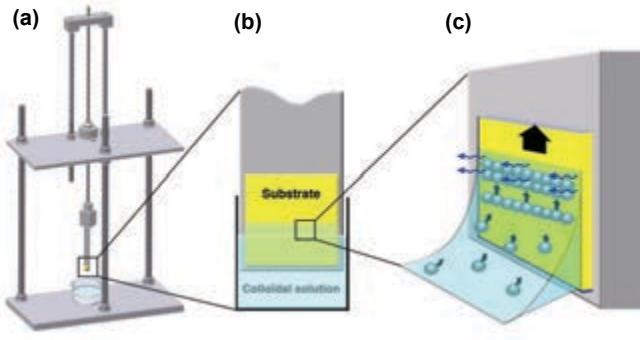

Figure 1: **(a)** Sketch of the home-made dip coating setup used in this work **(b)**. Schematic drawing of the situation at the beginning of the dip-coating process. **(c)** Schematic representation of MNPs accumulation and the flow pattern when the substrate is removed from the suspension.

Dip-coating experiments were performed using the home-made setup shown in Figure 1. The substrate is maintained with a small amount of vacuum grease on a cover slip. Such configuration enables an easy handling and prevents any deposit on the substrate backside, altering magnetic measurements performed on the final device. The

cover slip is maintained vertically using a self grip tweezer. The first step consists in completely immersing the substrate in a 1 mL teflon beaker filled beforehand with the suspension of MNPs. The substrate is then withdrawn vertically at a constant speed by action of a stepper motor at a speed ranging from 13 $\mu m.s^{-1}$ to 660 $\mu m.s^{-1}$.

Characterization of assemblies. Deposit patterns formed by the MNPs were imaged by optical microscope (Olympus BXFM) equipped with a CCD camera (Olympus DP20) integrated in the glove-box. Field emission gun scanning electron microscopy (SEM-FEG Hitachi S-4800) was performed at 30 KV. Topographical imaging of films was performed in tapping mode at room temperature with a Digital Instruments/Veeco Dimension 3100 Atomic Force Microscope using Si tips (frequency range: 240-380 kHz, Force: 42 $N.m^{-1}$). AFM image processing and rendering was analyzed with WsXM data analysis software.[41]
The magnetic properties of assemblies were investigated by using a superconducting quantum interference device (SQUID) magnetometer MPMS XL SQUID (7 T). Magnetization versus applied magnetic field curves were recorded at 2K without applying any magnetic field referred as ZFC (Zero field cooling). Then, the field cooling curves (FC) were recorded after the temperature was set down 2 K under 5 T. The substrates containing the assemblies of MNPs were placed in a parallel direction to the one of the applied magnetic field.

Results and discussions

Results

Core/shell carbide CoFe MNPs used hereafter exhibit a polydisperse size distribution with a diameter centered on 25.4 $\pm$ 9.7 nm and 14 $\pm$ 4 nm separated by organic ligands with a thickness distribution centered on 2.3 $\pm$ 1 nm (see Figure S1). STEM-HAADF images highlighted the polycrystalline morphology of the CoFe MNPs (see Figure S2 **(a-b)**) while STEM-EELS analysis evidenced a core-shell structure (respectively Co/Fe). It will be noted that the shell (see orange color in Figure S2 **(c)**) is very thin compared to the core. XRD measurements, used to characterize the phases present in a powder of CoFe MNPs, revealed that the crystallization of the core is a ε cobalt phase while the signature of Fe could be masked by the small size of crystallites and the strong signal of cobalt. Such unexpected phase suggests the presence of carbon formed during the synthesis, and its diffusion inside the MNPs structure confirmed by Mossbauer spectroscopy showing a carbide phase following a stoichiometry of $Fe_{1-x}Co_xC_y$ (see figure S3).
A powder sample exhibited a weak ferromagnetism character at 200 K as determined by SQUID magnetometry (M_S = 140 $A.m^2.kg^{-1}$, and H_C = 6 mT). The fact that the mean magnetization at saturation is below the expected value ($M_{S\ bulk}$ = 174 $A.m^2.kg^{-1}$) could be related to the presence of carbon inside the MNPs structure and/or carbon monoxide on the surfaces of the latters. The absence of a shift of the coercive field at 2 K after ZFC and FC (see Figure S4) confirms that the MNPs are not oxidized after synthesis.

MNPs concentration

We investigated the effect of the concentration of the CoFe MNP suspension on the deposit pattern. The concentration was varied from [5 $mmol.L^{-1}$] to [50 $mmol.L^{-1}$]. The minimum value was limited by the accuracy of the microbalance giving an error around 15 %, while the highest concentration was the threshold above which the MNPs were not effectively stabilized in the solvent. Except for the highest concentration, colloidal solution were stable for several hours, much longer than dip coating experiments ($\approx$ 6 min per deposit).

Figure 2 **(a)** depicts optical images of four deposits obtained respectively for 5, 10, 20 and 50 $mmol.L^{-1}$ at a fixed withdrawal speed (13 $\mu m.s^{-1}$). Corresponding scanning electron microscopy (SEM) images taken in random areas are shown in Figure S5. Formation of stripe patterned layer, perpendicular to the withdrawal direction (horizontal on the images) was observed for each sample. The width and spacing of the stripes could be monotonically tuned by the concentration of the CoFe MNP suspensions as evidenced in Figure 2 **(b)**. We observed an increase of the averaged width as well as the stripes spacing

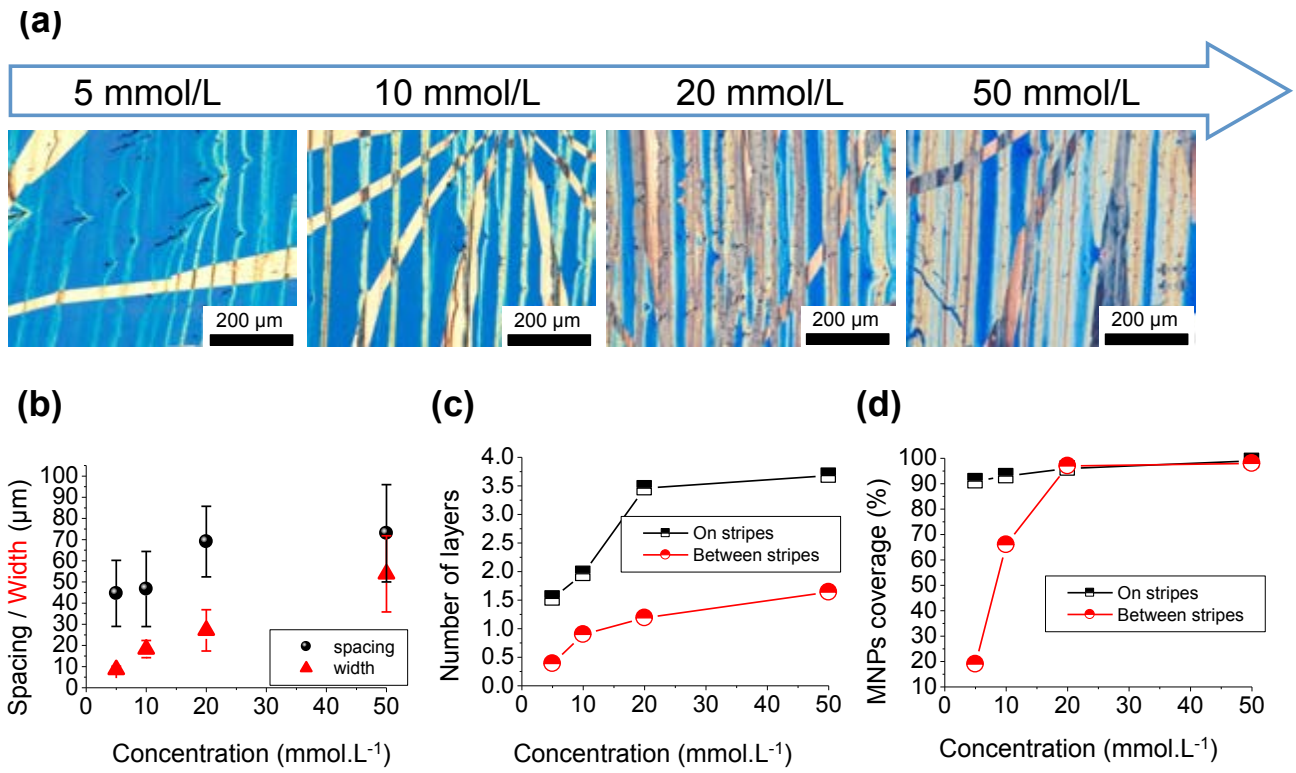

Figure 2: **(a)** Optical images of the stripe patterns formed perpendicularly to the withdrawal direction on the silicon oxide and gold electrodes. All deposits were performed at constant withdrawal speed ($13\ \mu m.s^{-1}$) for different MNP concentration: 5, 10, 20 and $[50\ mmol.L^{-1}]$. **(b)** Summary of the averaged width of the stripes (red triangles) and the average spacing between the consecutive stripes (black circles). The error bars correspond to statistical dispersion of the measurements performed on the entire surface of the substrates. **(c)**-**(d)** Summary of respectively the mean number of layers and the MNP coverage (deduced from AFM measurements) as a function of the concentration.

when the MNP concentration increases, similarly to what can be found in the literature.[42] Thickness of the deposit, quantified in number of layers, was evaluated from AFM images both on stripes or in between, depicted respectively in black or red in Figure S6.

For the lowest MNP concentration (see the Figure S6 **(a)**), thickness of a quarter of a layer was detected, corresponding to the substrate roughness between stripes, thus, no MNPs deposit. This roughness must be removed from further quantitative analysis. To further quantify the results obtained, two parameters were introduced *i)* the mean number of layers $\bar{N_L}$ (Figure 2 **c**)) which can be quantified by:

$$\bar{N_L} = \int \frac{N_L \times Ptot(N_L)}{P_{tot}(N_L)} \mathrm{d}N_L \qquad (1)$$

and ii) the MNP coverage Γ (Figure 2 **d**)) corresponding to:

$$\Gamma = \int \frac{P_{MNP}(N_L)}{P_{tot}(N_L)} \mathrm{d}N_L \times 100\% \qquad (2)$$

where N_L, $P_{MNP}(N_L)$ and $P_{tot}(N_L)$ are respectively the distribution of the number of layers, the probability corresponding to the distribution of the number of layers without the peak corresponding to the substrate roughness (i.e the absence of MNPs) and the probability of the entire distribution.

The mean number of layers increases with the MNP concentration both within or in between stripes, respectively black and red symbols. A plateau seems to appear for stripes of 3.5 layers above $[20\ mmol.L^{-1}]$. In agreement, the MNP coverage evolves toward a dense deposit (100% coverage) at high concentration. Above $[50\ mmol.L^{-1}]$, dense layer could be deposited but stripes were composed of multilayers (3 to 4). The almost linear increase of the mean number of layers (for the three lowest concentration) as well

as a high and almost constant MNP coverage are in perfect agreement with the literature.[21,43] The deviation observed at the highest concentration, could be understood by the unstable character of the colloidal suspension, the actual concentration of suspended MNPs being lower than the calculated one. Another hypothesis would be that, since the static contact angle formed by a droplet of THF on our substrates is very low (≈ 7 °), the thickness of the stripes is limited at high concentration by the dynamic contact angle. This could clear up why the thickness saturates while the width of the stripes still growths.
In the seeking of an homogeneous monolayer deposition, consisting of a mean thickness of one, both on and between stripes with a high MNP coverage, the best compromise was obtained for a $[10\ mmol.L^{-1}]$ concentration. This concentration was kept constant for the rest of the study.

Withdrawal speed

We have studied the impact of withdrawal speed on the deposit properties. Experiments have been performed for $[10\ mmol.L^{-1}]$ concentration at respectively 0, corresponding to the natural evaporation of the MNP solution,13, 15, 19, 29 and 180 $\mu m.s^{-1}$. Except for the highest withdrawal speed, which exhibited clusters of a few isolated MNPs induced by the strong stretching of the meniscus,[44] stripe patterned layer perpendicular to the withdrawal direction were detected from optical and SEM images (Figure 3 **(a)**), similarly to the MNP concentration study.

Figure 3 **(b)** summarizes the evolution of the width and the spacing of the stripes (respectively black squares and red triangles). The stripe width decreased exponentially with withdrawal speed, as previously reported.[44] Concerning the spacing of the stripes, previous works have shown two behaviors. On one hand, an almost constant spacing with the withdrawal speed (measured for a speed below $\approx$ 3 $\mu m.s^{-1}$)[42,44] have been recently reported. On the other hand, a non-monotonous behaviour against the withdrawal speed was exhibited on a broader range (below $\approx$ 150 $\mu m.s^{-1}$).[45] The fast withdrawal induced a shorter accumulation time of MNPs at the contact line, resulting in thinner stripes. As expected, mean number of layers decreased also drastically both in and between stripes (Figure 3 **(c)**) as well as the density of the deposit, evaluated by the MNP coverage parameter (Figure 4 and Supplementary Figure S7). Stripe width and thickness and MNP coverage evolved similarly towards a diminution for higher withdrawal speed. However, transition could be observed from an "evaporation" regime at low speed, with large and thick stripes, to an "intermediate regime", with a weak dependence of the stripe width with withdrawal speed associated to a low thickness.[40,46,47]

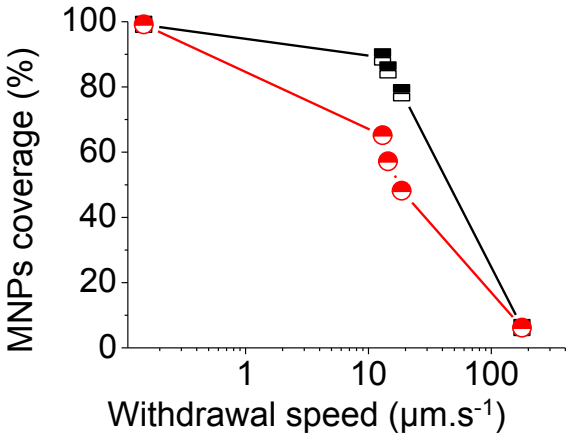

Figure 4: Evolution against the withdrawal speed of the MNP coverage deduced from AFM measurements (see Figure S7). Black (red) curves represent MNP coverage on (between) stripes.

Figure 4 shows the evolution of the MNP coverage on and between stripes (respectively black and red curves) deduced from AFM measurements against the withdrawal speed (see Figure S7) using Equ.(2) and the methodology described in the previous part. The MNP coverage presents both on and between stripes a monotonous decrease with increasing withdrawal speed.
13 $\mu m.s^{-1}$ speed appeared as the best compromise to control the deposit thickness, close to a monolayer in and between stripes, while providing the best MNP coverage (65 %). This withdrawal speed will be kept constant for the rest of the study.

Surfactants concentration

The impact of surfactants was systematically studied through the controlled addition of amine

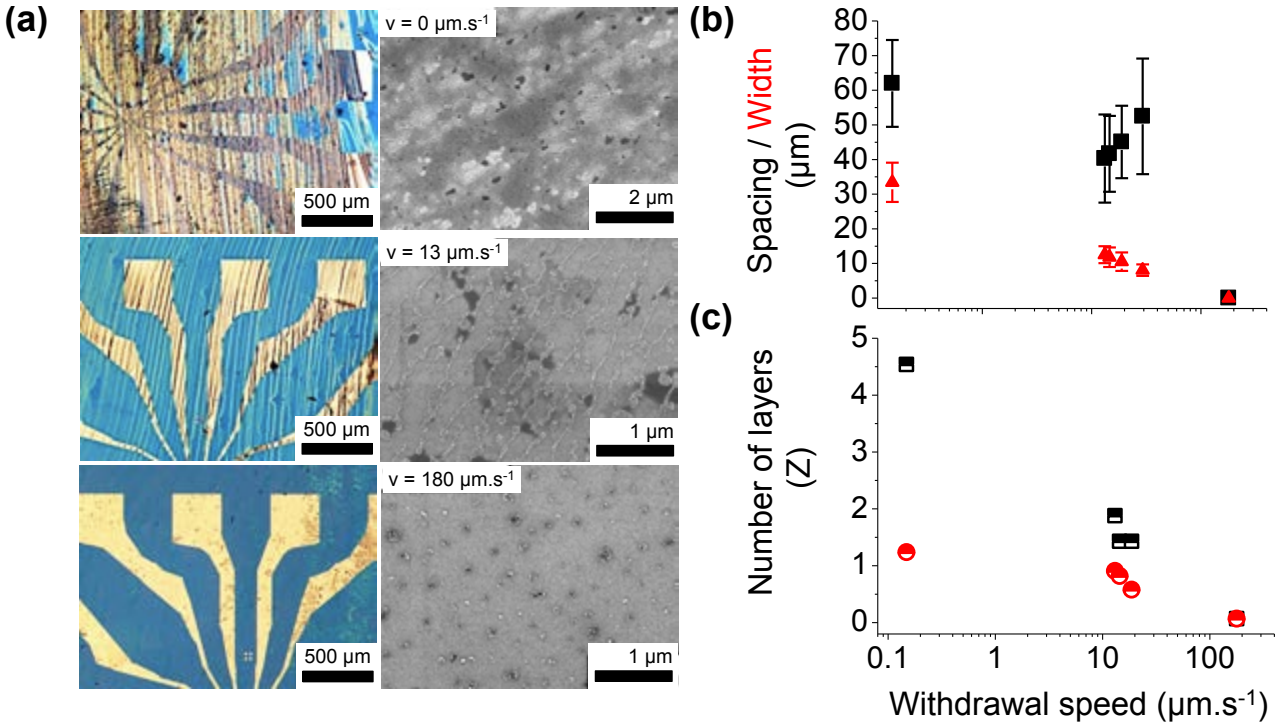

Figure 3: **(a)** Representative images of the stripes obtained by the dip coating method at different withdrawal speeds (vertically downwards, at zero withdrawal speed (corresponding to the natural evaporation of the MNP suspension), 13 $\mu m.s^{-1}$ and 180 $\mu m.s^{-1}$). MNP concentration was ($[10\ mmol.L^{-1}]$). The left column corresponds to optical images. The right column shows SEM images of a zone located on the silica layer between two consecutive stripes. **(b)** Evolution of the spacing (black squares) and the width (red triangles) of consecutive stripes with the withdrawal speed. Error bars correspond to the statistical dispersion of measurements performed on all of the substrate (5 mm). **(c)** Evolution of the mean number of layers of the stripes against the withdrawal speed. Black (red) curves represent the mean MNP coverage on (between) stripes.

(hexadecylamine - HDA) or acid (oleic acid - OA). The chemical affinities of surfactants with silica substrate or gold electrodes was investigated by immersing substrates separately into $[10\ mmol.L^{-1}]$ solution of OA and HDA in THF (Figure S8). While a reference sample in THF reveals an homogeneous contrast (Figure S8 **(c)**), the presence of OA (liquid at room temperature) leaded to multiple droplets randomly distributed on both silica and gold (Figure S8 **(a)**) while HDA (solid) was solely observed on and at the vicinity of gold electrodes (see Figure S8 **(b)**). While both amine and carboxylic groups of acid can form self-assembled monolayers on gold surfaces in low-polar solvent,[48,49] the affinity of surfactants with silica strongly depends of the substrate pending group. Silanol (Si-OH) could form hydrogen bonds with both surfactants, while only acid could interact with siloxane bridges (Si-O-Si), thus amine exhibit a lower reactivity towards silica compared to acid.

We then studied the influence of the ligand concentration on the MNP deposit at optimized speed (13 μms^{-1}) and concentration $[10\ mmol.L^{-1}]$. Controlled concentration of surfactants (varying from 0 to $[10\ mmol.L^{-1}]$, referred to as 1 equivalent per mole of metal, eq.) were added to the colloidal solution and sonicated for 15 min. Optical images revealed a clear evolution of the color of the deposits, while SEM images addressed the deposit morphology (Figure 5).

In presence of OA, MNP coverage decreased, 3D isolated islands and regions evidenced by a black contrast in SEM images, probably filled with organic molecules, arisen both on Au and SiO_2 surface (Figure S8 **(a)**). While the same behaviour was observed in presence of HDA on Au electrodes, the MNP coverage on SiO_2 increases with HDA (Figure 5 and Figure S9). Ligand physisorption, enhanced at the three-phase contact line,

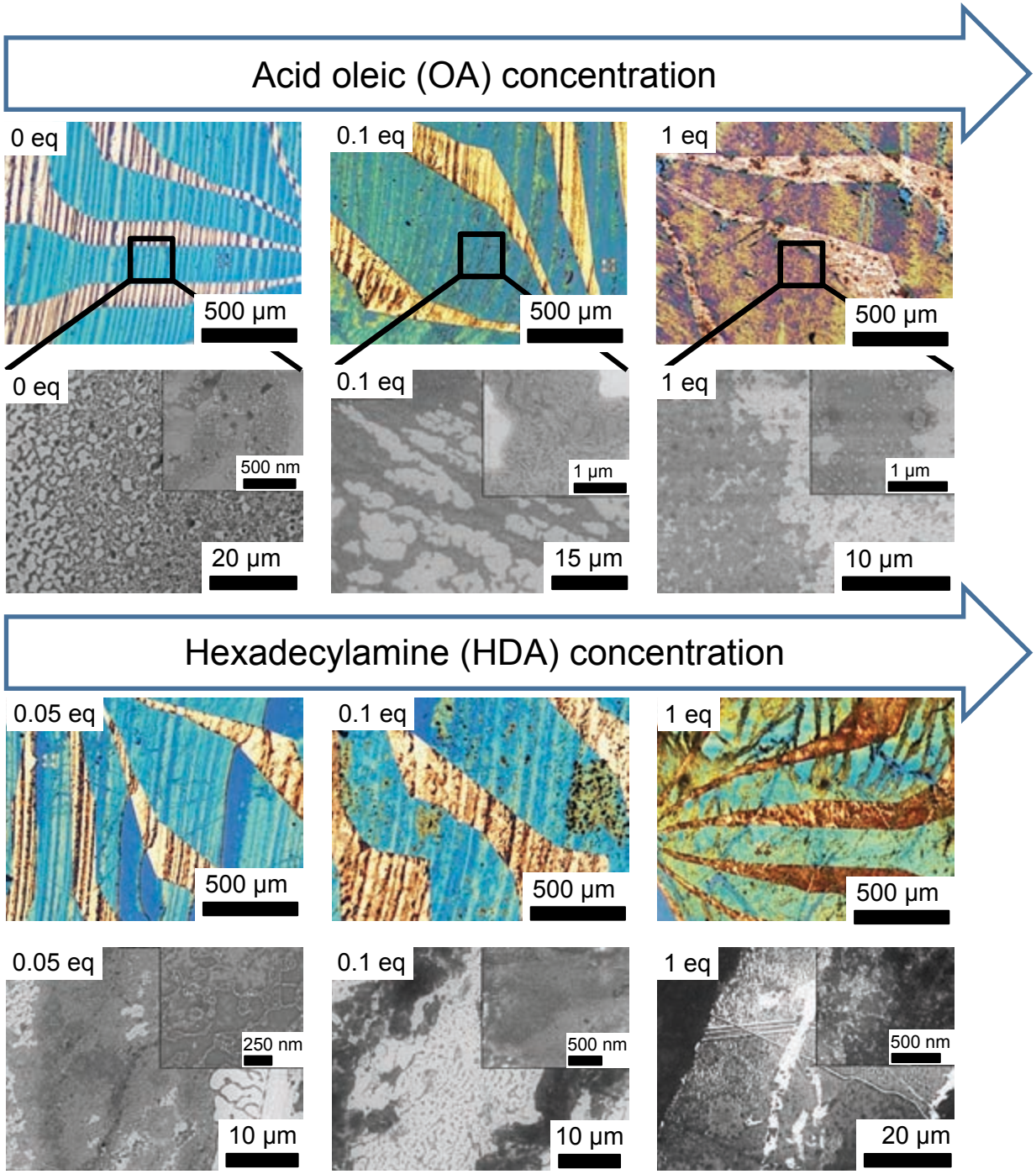

Figure 5: Optical and SEM images of the deposits obtained by the dip coating method at the optimized speed ($v = 13\ \mu m.s^{-1}$). The concentration of the surfactants has been varied by adding the latters in a powder form directly inside the colloidal suspensions of CoFe MNPs beforehand prepared at optimized concentrations ($[X] = [10\ mmol.L^{-1}]$). Excess amount of **(a)** 0, 0.1 and 1 equivalent of OA and **(b)** 0.05, 0.1 and 1 equivalent of HDA has been added. All SEM images are located on silica and endowed, in inset, with magnified view.

could form a shear barrier to prevent MNPs interaction with the surface, decreasing the MNP coverage.[35,50,51] In the case of low affinity between the surfactants and the surface, no steric hindrance were encountered, as evidenced for HDA on SiO_2. Surfactants could enhance the MNPs-MNPs interactions as well as the depletion force, increasing the MNP coverage as previously reported.[23,52]

Surface energy of the substrates

We studied so far the deposition on silica and gold surfaces beforehand cleaned by ultraviolet (UV)/ozone and then stored inside the glove box. However, the surface state evolved as evidenced by the drastic increase of the contact angle of deionized water from 10 ° and reach 60 ° after 6 hours (Figure S10). Such evolution is probably due to the physisorption of organic molecules or contaminants. To address the effect of surface energy and solvent wettability issue we performed oxygen plasma treatment of different time. Dip coating of treated substrate were performed under optimized conditions ($v = 13\ \mu m.s^{-1}$ and $[X] = [10\ mmol.L^{-1}]$).

For long plasma treatment stripes were less visible, suggesting that the deposition mechanism is close to a thin film entrainment (Figure 6). SEM images confirmed that MNP coverage significantly increased compared to a deposit on bare substrate (Figure S5 **(b)**) for comparison). Such enhancement of the MNP coverage could be explained by *i)* the removing of physisorbed molecules which, as previously discussed, decrease the interaction energy between the MNPs and the substrate,[35] and/or *ii)* a lower contact angle, which permits a higher evaporation rate and a homogeneous thickness of the deposit.[53]

Concerning this last point, the average spacing between two successive stripes as well as the width of the stripes increases nonlinearly with the oxygen plasma treatment duration (Figure 7). Such experiments demonstrates indirectly the decrease of the contact angle acting on the triple line. Indeed, a smaller contact angle (for a fixed withdrawal speed) is known to avoid the MNPs to diffuse toward to the triple contact line and entails that the next stripe starts its formation farther (*i.e* the average spacing increases).[54] Moreover, it has been shown that a low contact angle provide a convective self-assembly with wider stripes, while increasing contact angle progressively forms incompletely layers with defects until prevent MNPs from being deposited on the substrates when the contact angle reaches around 20 °.[55]
To conclude on that point, the increase of the average spacing between two consecutive stripes combined to an increase of the widths constitute a fingerprint of the decrease of the contact angle when the oxygen plasma treatment duration is longer.

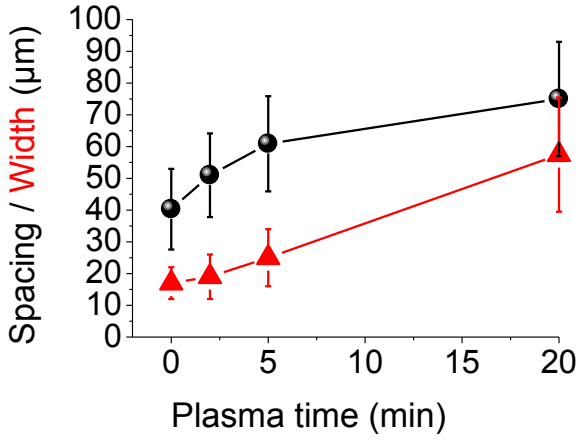

Figure 7: Evolution of the spacing (black circles) and the width (red triangles) of consecutive stripes against the oxygen plasma treatment for different exposition durations. The first point (t = 0) is the reference for this study, where a substrate of the same batch was stored in the glovebox at least for one day without oxygen plasma treatment. Error bars correspond to the statistical dispersion of measurements performed on all the substrate (5 mm).

The intrinsic magnetic character of the CoFe MNPs used in this work could also be an important factor guiding the self-assembly through magnetostatic dipole-dipole interactions (U). In particular, it has been shown that, for $U > 8\ k_BT$, characteristic and noticeable self-organizations of MNPs are observed (rings, chains, ...[56]). In our case, one can estimate the dipolar energy between two MNPs i and j using $U \approx (\mu_i\mu_j)/\sigma_{i,j}^3$ where $\mu_i = M_sV_i$ is the magnetization carried by a MNP i of volume V_i and $\sigma_{i,j}$ the center-to-center distance between the MNPs i and j. Due to the bidisperse character of the MNPs (displayed on their size distribution in Figure S1), we obtain U $\approx$ 124 and 316 k_BT for the small and the larges MNPs respectively. Despite these large values of $(U >> k_BT)$, we never clearly observed the characteristic structures induced by a self-assembly governed by dipolar interactions.[56]
In fact, many theoretical works demonstrated that the probability of forming MNPs chains are strongly reduced in bimodal systems compared

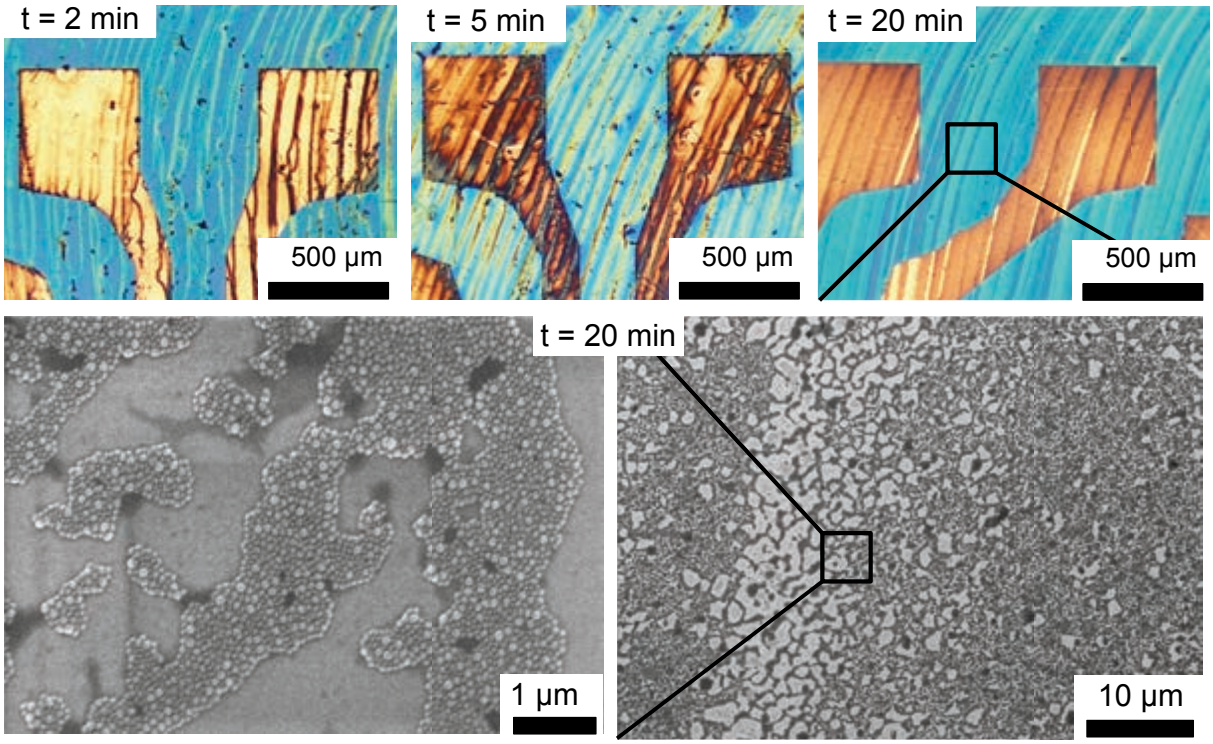

Figure 6: Optical images of samples deposited after different oxygen plasma treatment durations : 2 min, 5 min and 20 min respectively from the left to the right. Other conditions are $v = 13\ \mu m.s^{-1}$ and $[X] = [\,10 mmol.L^{-1}]$). On the bottom, high resolution SEM images located on silica for the longest plasma treatment are shown.

to monodisperse ones.[57–59] This can be qualitatively explained by the presence of the small MNPs which *i/* lowered the effective dipolar interactions seen by the larges MNPs, and *ii/* increase the breakup probability of long chains through their Brownian motion; both phenomena leading to only 2-3 MNPs aggregation.

Finally, magnetic measurements have been performed on a deposit of CoFe MNPs using the optimized conditions described above (speed 13 $\mu m.s^{-1}$, concentration 10 $mmol.L^{-1}$ on a silicon substrate with native thin oxide cleaned by plasma oxygen during 20 min). To preserve the magnetic properties of the MNPs, but also their geometrical arrangement after dip-coating, a thin resin layer ($\approx$ 40 nm thick) has been deposited followed by four annealing steps (1 min at 90°, 110°, 170°, 250°), still inside the glovebox (see Figure 8). The magnetic measurements have been performed with the magnetic field applied in the plane of the substrate. Interestingly, the hysteresis loops measured at 2 K after field cooling under 5 T did not exhibit any exchange bias features, meaning that no oxidation occurred during the whole process, *i.e* the magnetic properties of the MNPs are preserved. It will be noted that this deposition method was successfully extended to MNPs displaying monodisperse size distribution for different materials, ligands and to various type of substrates. These latter works will be reported elsewhere.

Outline

In conclusion, we have systematically investigated the influence of MNP concentration, withdrawal speed, nature/concentration of the surfactants and the surface state of the substrates on the deposit obtained by dip-coating technique. We successfully performed deposition of metallic magnetic MNPs on hydrophilic surfaces under inert atmosphere thanks to an home-made set-up designed in a couple glovebox-sputtering system, to prevent

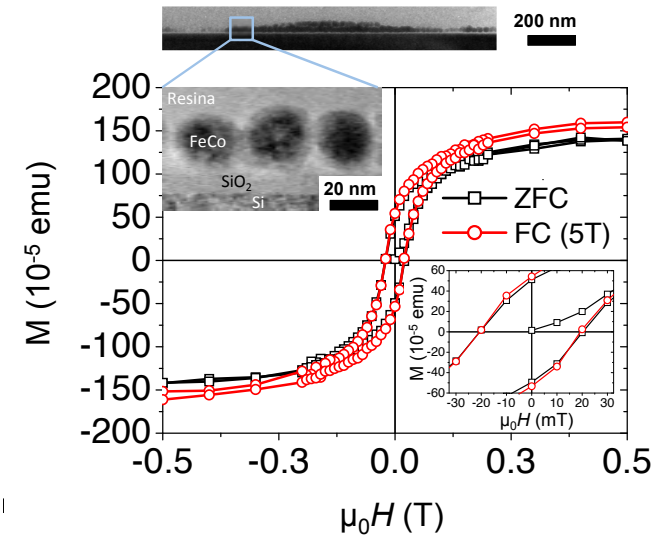

Figure 8: At the top, a cross section TEM picture of the sample used for the magnetic measurements. On the bottom: in-plane hysteresis loops of the sample measured at 2K after zero-field cooling (ZFC) (black squares) and after field-cooling (FC) under 5T (red circles).

any oxidation of the deposit. The film thickness can be controlled by either the MNP concentration or the withdrawal speed. Deposition of single monolayers could be reached for a concentration of $[X] = [10\ mmol.L^{-1}]$ and a withdrawal speed $v = 13\ \mu m.s^{-1}$. On contrary, very thick periodic stripes can be formed either at high MNP concentration or without any withdrawal force, corresponding to the natural evaporation of the MNP suspension. By adding surfactants containing amino and acid groups in two distinct freshly synthesized suspensions, we have demonstrated how drastically the nature and the amount of such surfactants modifies the morphology of the deposit. For surfactants strongly interacting with the surface, lower MNP coverage were obtained, physisorbed surfactants acting as shearing barrier towards MNP adhesion. When surfactants do not exhibit preferential interaction, for instance for HDA on SiO_2, improved coverage were obtained, probably due to the enhancement of MNPs-MNPs interactions and depletion force in suspension. A 20 min plasma treatment of the samples prior to dip-coating yield the highest MNP coverage.
Interestingly, those preliminary experiments permits to achieve dense monolayer of monodisperse MNPs (Fe, Co, CoFe) on silica surfaces functionalized by APTES molecules, gold surfaces as well as thin resina layer while preserving the magnetic properties of the MNPs which will be published elsewhere.

Supporting Information Available

Additional experimental results are available. Structural analysis ((1) TEM, size distribution, (2) STEM-HAADF, STEM-EELS, Powder XRD patterns, (3) Mossbauer) of CoFe MNPs. (4) Magnetic properties of a powder of CoFe MNPs measured at different temperature without magnetic field and under 5 T merely at 2 K. (5) SEM characterization taken after the deposition at different concentration. (6-7) AFM measurements performed at different MNP concentration and withdrawal speed. (8) Optical images taken after the substrates were immersed in suspensions of OA and HDA dissolved in THF as well as pure THF. (9) A high resolution SEM image located between two consecutive stripes when a large excess of HDA (1 eq) were added to the suspension. (10) Evolution against the time of the contact angle of cleaned substrates and then stored in glovebox.

Acknowledgement

This work was partly supported by the CNRS LAAS member of french RENATECH network. The authors gratefully acknowledge C.Nayral and F.Delpech for fruitful discussions.

References

(1) Whitesides, G. M.; Grzybowski, B. Self-Assembly at All Scales. *Science* **2002**, *295*, 2418–2421.

(2) Talapin, D. V.; Lee, J.; Kovalenko, M. V.; Shevchenko, E. V. Prospects of Colloidal Nanocrystals for Electronic and Optoelectronic Applications. *Chemical Reviews* **2010**, *110*, 389–458.

(3) Reiss, G.; Hütten, A. Magnetic nanoparticles: Applications beyond data storage. *Nature Materials* **2005**, *4*, 725–726.

(4) Chappert, C.; Fert, A.; Van Dau, F. N. The emergence of spin electronics in data storage. *Nat Mater* **2007**, *6*, 813–823.

(5) Tan, R. P.; Carrey, J.; Desvaux, C.; Grisolia, J.; Renaud, P.; Chaudret, B.; Respaud, M. Transport in Superlattices of Magnetic Nanoparticles: Coulomb Blockade, Hysteresis, and Switching Induced by a Magnetic Field. *Phys. Rev. Lett.* **2007**, *99*, 176805.

(6) Dugay, J.; Tan, R. P.; Meffre, A.; Blon, T.; Lacroix, L.; Carrey, J.; Fazzini, P. F.; Lachaize, S.; Chaudret, B.; Respaud, M. Room-Temperature Tunnel Magnetoresistance in Self-Assembled Chemically Synthesized Metallic Iron Nanoparticles. *Nano Letters* **2011**, *11*, 5128–5134.

(7) Koh, S. Strategies for Controlled Placement of Nanoscale Building Blocks. *Nanoscale Research Letters* **2007**, *2*, 519–545.

(8) Tan, R. P.; Lee, J. S.; Cho, J. U.; Noh, S. J.; Kim, D. K.; Kim, Y. K. Numerical simulations of collective magnetic properties and magnetoresistance in 2D ferromagnetic nanoparticle arrays. *Journal of Physics D: Applied Physics* **2010**, *43*, 165002.

(9) Tran, T. B.; Beloborodov, I. S.; Hu, J.; Lin, X. M.; Rosenbaum, T. F.; Jaeger, H. M. Sequential tunneling and inelastic cotunneling in nanoparticle arrays. *Phys. Rev. B* **2008**, *78*, 075437.

(10) Pauly, M.; Dayen, J.; Golubev, D.; Beaufrand, J.; Pichon, B. P.; Doudin, B.; Bégin-Colin, S. Co-tunneling Enhancement of the Electrical Response of Nanoparticle Networks. *Small* **2012**, *8*, 108–115.

(11) Cui, Y.; Björk, M. T.; Liddle, J. A.; Sönnichsen, C.; Boussert, B.; Alivisatos, A. P. Integration of Colloidal Nanocrystals into Lithographically Patterned Devices. *Nano Letters* **2004**, *4*, 1093–1098.

(12) Dai, Q.; Chen, Y.; Liu, C.; Rettner, C. T.; Holmdahl, B.; Gleixner, S.; Chung, R.; Pitera, J. W.; Cheng, J.; Nelson, A. Programmable Nanoparticle Ensembles via High-Throughput Directed Self-Assembly. *Langmuir* **2013**,

(13) Guo, Q.; Teng, X.; Yang, H. Fabrication of Magnetic FePt Patterns from Langmuir–Blodgett Films of Platinum–Iron Oxide Core–Shell Nanoparticles. *Advanced Materials* **2004**, *16*, 1337–1341.

(14) Park, J.; Lee, W.; Bae, S.; Kim, Y. J.; Yoo, K.; Cheon, J.; Kim, S. Langmuir Monolayers of Co Nanoparticles and Their Patterning by Microcontact Printing. *The Journal of Physical Chemistry B* **2005**, *109*, 13119–13123.

(15) Kraus, T.; Malaquin, L.; Schmid, H.; Riess, W.; Spencer, N. D.; Wolf, H. Nanoparticle printing with single-particle resolution. *Nat Nano* **2007**, *2*, 570–576.

(16) Jie, Y.; Niskala, J. R.; Johnston-Peck, A. C.; Krommenhoek, P. J.; Tracy, J. B.; Fan, H.; You, W. Laterally patterned magnetic nanoparticles. *Journal of Materials Chemistry* **2012**, *22*, 1962.

(17) Cavallini, M.; Bystrenova, E.; Timko, M.; Koneracka, M.; Zavisova, V.; Kopcansky, P. Multiple-length-scale patterning of magnetic nanoparticles by stamp assisted deposition. *Journal of Physics: Condensed Matter* **2008**, *20*, 204144.

(18) Basnar, B.; Willner, I. Dip-Pen-Nanolithographic Patterning of Metallic, Semiconductor, and Metal Oxide Nanostructures on Surfaces. *Small* **2009**, *5*, 28–44.

(19) Bellido, E.; Ojea-Jiménez, I.; Ghirri, A.; Alvino, C.; Candini, A.; Puntes, V.; Affronte, M.; Domingo, N.; Ruiz-Molina, D. Controlled Positioning of Nanoparticles on Graphene by Noninvasive AFM Lithography. *Langmuir* **2012**, *28*, 12400–12409.

(20) Krämer, S.; Fuierer, R. R.; Gorman, C. B. Scanning Probe Lithography Using Self-Assembled Monolayers. *Chemical Reviews* **2003**, *103*, 4367–4418.

(21) Fustin, C.; Glasser, G.; Spiess, H. W.; Jonas, U. Parameters Influencing the Templated Growth of Colloidal Crystals on Chemically Patterned Surfaces. *Langmuir* **2004**, *20*, 9114–9123.

(22) Ma, L.; Subramanian, R.; Huang, H.; Ray, V.; Kim, C.; Koh, S. J. Electrostatic Funneling for Precise Nanoparticle Placement: A Route to Wafer-Scale Integration. *Nano Letters* **2007**, *7*, 439–445.

(23) Bigioni, T. P.; Lin, X.; Nguyen, T. T.; Corwin, E. I.; Witten, T. A.; Jaeger, H. M. Kinetically driven self assembly of highly ordered nanoparticle monolayers. *Nat Mater* **2006**, *5*, 265–270.

(24) Adachi, E.; Dimitrov, A. S.; Nagayama, K. Stripe Patterns Formed on a Glass Surface during Droplet Evaporation. *Langmuir* **1995**, *11*, 1057–1060.

(25) Dong, A.; Ye, X.; Chen, J.; Murray, C. B. Two-Dimensional Binary and Ternary Nanocrystal Superlattices: The Case of Monolayers and Bilayers. *Nano Letters* **2011**, *11*, 1804–1809.

(26) Dong, A.; Chen, J.; Oh, S. J.; Koh, W.-k.; Xiu, F.; Ye, X.; Ko, D.; Wang, K. L.; Kagan, C. R.; Murray, C. B. Multiscale Periodic Assembly of Striped Nanocrystal Superlattice Films on a Liquid Surface. *Nano Letters* **2011**, *11*, 841–846.

(27) Aleksandrovic, V.; Greshnykh, D.; Randjelovic, I.; Frömsdorf, A.; Kornowski, A.; Roth, S. V.; Klinke, C.; Weller, H. Preparation and Electrical Properties of Cobalt-Platinum Nanoparticle Monolayers Deposited by the Langmuir-Blodgett Technique. *ACS Nano* **2008**, *2*, 1123–1130.

(28) Huang, J.; Kim, F.; Tao, A. R.; Connor, S.; Yang, P. Spontaneous formation of nanoparticle stripe patterns through dewetting. *Nat Mater* **2005**, *4*, 896–900.

(29) Bodnarchuk, M. I.; Kovalenko, M. V.; Heiss, W.; Talapin, D. V. Energetic and Entropic Contributions to Self-Assembly of Binary Nanocrystal Superlattices: Temperature as the Structure-Directing Factor. *Journal of the American Chemical Society* **2010**, *132*, 11967–11977.

(30) Farcau, C.; Moreira, H.; Viallet, B.; Grisolia, J.; Ressier, L. Tunable Conductive Nanoparticle Wire Arrays Fabricated by Convective Self-Assembly on Nonpatterned Substrates. *ACS Nano* **2010**, *4*, 7275–7282.

(31) Johnston-Peck, A. C.; Wang, J.; Tracy, J. B. Formation and Grain Analysis of Spin-Cast Magnetic Nanoparticle Monolayers. *Langmuir* **2011**, *27*, 5040–5046.

(32) Lu, A.; Salabas, E. L.; Schüth, F. Magnetic Nanoparticles: Synthesis, Protection, Functionalization, and Application. *Angewandte Chemie International Edition* **2007**, *46*, 1222–1244.

(33) Chaudret, B. Organometallic approach to nanoparticles synthesis and self-organization. *Comptes Rendus Physique* **2005**, *6*, 117 – 131.

(34) Yin, Y.; Alivisatos, A. P. Colloidal nanocrystal synthesis and the organic-inorganic interface. *Nature* **2005**, *437*, 664–670.

(35) Kwon, C.; Yoon, T.; Yim, S.; Park, S.; Kim, K. The effect of excess surfactants on the adsorption of iron oxide nanoparticles during a dip-coating process. *Journal of Nanoparticle Research* **2009**, *11*, 831–839.

(36) Desvaux, C.; Dumestre, F.; Amiens, C.; Respaud, M.; Lecante, P.; Snoeck, E.; Fejes, P.; Renaud, P.; Chaudret, B. FeCo nanoparticles from an organometallic approach: synthesis, organisation and physical properties. *Journal of Materials Chemistry* **2009**, *19*, 3268–3275.

(37) Rasband, Rasband, W.S., 1997. ImageJ, U.S. National Institutes of Health, Bethesda, Maryland, USA. **1997**,

(38) Smallwood, I. M. Handbook of Organic Solvents Halsted Press. *New York* **1996**, 178.

(39) Jang, J.; Nam, S.; Im, K.; Hur, J.; Cha, S. N.; Kim, J.; Son, H. B.; Suh, H.; Loth, M. A.; Anthony, J. E.; Park, J.; Park, C. E.; Kim, J. M.; Kim, K. Highly Crystalline Soluble Acene Crystal Arrays for Organic Transistors: Mechanism of Crystal Growth During Dip-Coating. *Advanced Functional Materials* **2012**, *22*, 1005–1014.

(40) Grosso, D. How to exploit the full potential of the dip-coating process to better control film formation. *J. Mater. Chem.* **2011**, *21*, 17033–17038.

(41) Horcas, I.; Fernandez, R.; Gomez-Rodriguez, J. M.; Colchero, J.; Gomez-Herrero, J.; Baro, A. M. WSXM: A software for scanning probe microscopy and a tool for nanotechnology. *Review of Scientific Instruments* **2007**, *78*, 013705.

(42) Watanabe, S.; Inukai, K.; Mizuta, S.; Miyahara, M. T. Mechanism for stripe pattern formation on hydrophilic surfaces by using convective self-assembly. *Langmuir* **2009**, *25*, 7287–7295.

(43) Kim, M. H.; Im, S. H.; Park, O. O. Rapid Fabrication of Two- and Three-Dimensional Colloidal Crystal Films via Confined Convective Assembly. *Advanced Functional Materials* **2005**, *15*, 1329–1335.

(44) Ghosh, M.; Fan, F.; Stebe, K. J. Spontaneous Pattern Formation by Dip Coating of Colloidal Suspensions on Homogeneous Surfaces. *Langmuir* **2007**, *23*, 2180–2183.

(45) Yabu, H.; Shimomura, M. Preparation of Self-Organized Mesoscale Polymer Patterns on a Solid Substrate: Continuous Pattern Formation from a Receding Meniscus. *Advanced Functional Materials* **2005**, *15*, 575–581.

(46) Le Berre, M.; Chen, Y.; Baigl, D. From Convective Assembly to Landau-Levich Deposition of Multilayered Phospholipid Films of Controlled Thickness. *Langmuir* **2009**, *25*, 2554–2557.

(47) Jing, G.; Bodiguel, H.; Doumenc, F.; Sultan, E.; Guerrier, B. Drying of Colloidal Suspensions and Polymer Solutions near the Contact Line: Deposit Thickness at Low Capillary Number. *Langmuir* **2010**, *26*, 2288–2293.

(48) Paik, W.-k.; Han, S.; Shin, W.; Kim, Y. Adsorption of Carboxylic Acids on Gold by Anodic Reaction. *Langmuir* **2003**, *19*, 4211–4216.

(49) Xu, C.; Sun, L.; Kepley, L. J.; Crooks, R. M.; Ricco, A. J. Molecular interactions between organized, surface-confined monolayers and vapor-phase probe molecules. 6. In-situ FT-IR external reflectance spectroscopy of monolayer adsorption and reaction chemistry. *Analytical Chemistry* **1993**, *65*, 2102–2107.

(50) Yoon, T.; Oh, J.; Park, S.; Kim, V.; Jung, B. G.; Min, S.; Park, J.; Hyeon, T.; Kim, K. Single and Multiple-Step Dip-Coating of Colloidal Maghemite ($\gamma - Fe_2O_3$) Nanoparticles onto Si, Si_3N_4, and SiO_2 Substrates. *Advanced Functional Materials* **2004**, *14*, 1062–1068.

(51) Wang, H.; Wang, H.; Yang, F.; Zhang, J.; Li, Q.; Zhou, M.; Jiang, Y. Deposition and characterization of large-scale FePt nanoparticle monolayers on SiO2/Si surface. *Surface and Coatings Technology* **2010**, *204*, 1509 – 1513.

(52) Lau, C. Y.; Duan, H.; Wang, F.; He, C. B.; Low, H. Y.; Yang, J. K. W. Enhanced Ordering in Gold Nanoparticles Self-Assembly through Excess Free Ligands. *Langmuir* **2011**, *27*, 3355–3360.

(53) Monteux, C.; Lequeux, F. Packing and Sorting Colloids at the Contact Line of a Drying Drop. *Langmuir* **2011**, *27*, 2917–2922.

(54) Ray, M. A.; Kim, H.; Jia, L. Dynamic Self-Assembly of Polymer Colloids To Form Linear Patterns. *Langmuir* **2005**, *21*, 4786–4789.

(55) Malaquin, L.; Kraus, T.; Schmid, H.; Delamarche, E.; Wolf, H. Controlled Particle

Placement through Convective and Capillary Assembly. *Langmuir* **2007**, *23*, 11513–11521.

(56) Bishop, K. J. M.; Wilmer, C. E.; Soh, S.; Grzybowski, B. A. Nanoscale Forces and Their Uses in Self-Assembly. *Small* **2009**, *5*, 1600–1630.

(57) Minina, E. S.; Muratova, A. B.; Cerdá, J. J.; Kantorovich, S. S. Microstructure of bidisperse ferrofluids in a thin layer. *Journal of Experimental and Theoretical Physics* **2013**, *116*, 424–441.

(58) Kruse, T.; Spanoudaki, A.; Pelster, R. Monte Carlo simulations of polydisperse ferrofluids: Cluster formation and field-dependent microstructure. *Physical Review B* **2003**, *68*, 054208.

(59) Wang, Z.; Holm, C. Structure and magnetic properties of polydisperse ferrofluids: A molecular dynamics study. *Physical Review E* **2003**, *68*, 041401.

Graphical TOC Entry